Bimetallic PdZn nanoparticles for oxygen reduction reaction in alkaline medium: The effects of surface structure

Hongyu Yang [a], Kai Wang [a], Zhenghua Tang [a,b,*], Zhen Liu [c], Shaowei Chen [a,d,*]

[a] Guangzhou Key Laboratory for Surface Chemistry of Energy Materials, New Energy Research Institute, School of Environment and Energy, South China University of Technology, Guangzhou Higher Education Mega Center, Guangzhou, Guangdong 510006, PR China
[b] Guangdong Engineering and Technology Research Center for Surface Chemistry of Energy Materials, School of Environment and Energy, South China University of Technology, Guangzhou Higher Education Mega Center, Guangzhou, Guangdong 510006, PR China
[c] Department of Physics & Engineering, Frostburg State University, Frostburg, MD 21532-2303, United States
[d] Department of Chemistry and Biochemistry, University of California, 1156 High Street, Santa Cruz, CA 95064, United States

ARTICLE INFO

ABSTRACT

Despite the recent advances in preparing high-efficiency and durable electrocatalysts for oxygen reduction reaction (ORR) toward fuel cell applications, there is still lacking of the understanding regarding the relationship between the electrocatalytic performance and the surface structure of the catalyst at atomic level. Herein, three PdZn bimetallic composites named as PdZn_Disordered, PdZn_Ordered and Pd@Zn_Core-shell (Pd: Zn = 1: 1) were prepared for ORR in alkaline medium to examine the surface structure effects. Multiple characterization means revealed that PdZn_Disordered and PdZn_Ordered had amorphous PdZn and ordered PdZn alloyed structure, respectively, while Pd@Zn_Core-shell held a Pd-core-ordered and Zn-shell-disordered architecture. In the electrochemical ORR tests, Pd@Zn_Core-shell exhibited the superior activity and stability in the series, outperforming the Pd/C and Pt/C catalysts. The electrocatalytic performance followed the order of Pd@Zn_Core-shell > PdZn_Ordered » PdZn_Disordered, which can be attributed to the effects of different surface structures of the catalysts.

© 2019 Elsevier Inc. All rights reserved.

1. Introduction

To alleviate our heavy reliance on environmental unfriendly fossil fuels, it is essential to explore new technologies for an efficient energy management. Proton exchange membrane fuel cells (PEMFCs) have been widely regarded as an ideal solution for sustainable energy storage and conversion thanks to their high efficiency, excellent reliability and negligible or even zero carbon oxides emission [1–3]. The energy conversion efficiency of PEMFCs is seriously restricted by the much slower oxygen reduction reaction (ORR) occurring at the cathode rather than the fast-going hydrogen oxidation reaction at the anode. The electrochemical reduction of oxygen follows different reaction mechanisms, depending on the pH value of the electrolyte. In acidic medium, the reaction formula is: $\mathbf{O_2 + 4H^+ + 4e \rightarrow 2H_2O}$, while for alkaline medium, the reaction follows the path of $\mathbf{O_2 + 2H_2O + 4e \rightarrow 4OH^-}$. The thermodynamic potentials (E^o) for ORR under standard condi-

tions are 1.229 V and 0.410 V for the above two pathways, respectively. The cathode material has a significant impact on the intermediate process of oxygen reduction. ORR can follow the direct efficient 4-electron transfer pathway, or the 2-step-2-electron transfer pathway (Acidic medium: $\mathbf{O_2 + 2H^+ + 2e \rightarrow H_2O_2}(E^o = 0.67\mathbf{V})$ and $\mathbf{H_2O_2 + 2H^+ + 2e \rightarrow 2H_2O}(E^o = 1.76\mathbf{V})$. Alkaline medium: $\mathbf{O_2 + H_2O + 2e \rightarrow HO_2^- + OH^-}(E^o = -0.065\mathbf{V})$ and $\mathbf{HO_2^- + H_2O + 2e \rightarrow 3OH^-}(E^o = 0.867\mathbf{V})$), where H_2O_2 or HO_2^- as byproduct is generated in the latter case [4–6]. As state-of-the-art ORR catalysts, Pt-based materials have attracted substantial research interests over the past decade [7–10]. However, such Pt-based catalysts suffer from the shortcomings of rare reserve of Pt in the Crust of Earth, high costs, and poor stability. These factors have become the primary barriers to the broad deployments and large-scale commercial applications of PEMFCs. To that end, it is pivotal to develop cost-effective, high-efficiency, and robust catalysts as alternative substitutes to meet the requirements for the profitable marketing [11–16].

Compared with platinum, palladium could be an attractive candidate which holds great promises to realize the industrial commercialization, thanks to the following factors. First of all,

* Corresponding authors.
  E-mail addresses: zhht@scut.edu.cn (Z. Tang), shaowei@ucsc.edu (S. Chen).

palladium has a much higher earth abundance than platinum in Earth's Crust. Secondly, palladium is an amazing metal which has shown exceptional catalytic activity in various reactions for commercial devices and industrial processes [17]. Finally and furthermore, palladium can readily be alloyed with other metals, especially transition metals, to form bimetallic nanostructures which further reduces the cost and significantly boosts its electrocatalytic performance. It is noted that the component ratios and atomic distributions of palladium and the transition metals can greatly affect the electrocatalytic activities of the bimetallic nanocrystals, as they can influence the electron transfer and coupling behaviors on the electrode surface. For instance, in terms of ORR, a variety of PdM (M = Transition metal) alloys including PdCu [18–20], PdFe [21,22], PdNi [23,24], PdCo [25,26], PdZn [21], PdCr [27], PdMo [27], PdW [27], and PdCuCo [28] have shown high catalytic activity and robust CO or methanol tolerance in fuel cells. The catalytic activity and long-term durability of these Pd-alloyed nanomaterials are at least comparable with, if not superior to, the state-of-the-art Pt/C catalyst [29].

Despite the impressive progresses, there is still a lack of fundamental understanding of PdM alloys regarding the basic science for the promotion effects at an atomic level. It is noted that the ORR electrocatalytic behavior is highly dependent on the surface structure of the catalyst, including the shape, the surface atomic mixing pattern, the crystal orientation, the surface structural defect and so on [30–33]. Several studies postulated that the enhanced ORR performance can be attributed to the altered kinetics or thermodynamics induced by the foreign atoms imparted on the Pd surface, but direct structural evidences are still missing [34]; Other researchers emphasized that the modulation of the electronic effects of the Pd surface could significantly affect the activity to some extent. However, besides X-ray photoelectron spectroscopy, developing advanced tools to corroborate such theory is still quite challenging [35–37]. To that end, the direct correlation between the surface structure and the electrocatalytic performance hasn't been well established. In light of the great influence of surface structure upon the catalytic performance, it is critical and imperative to systematically design PdM nanoparticles with different surface atomic structures to probe their catalytic performance, and eventually establish the structure-performance relationship. This is the primary goal of the current investigation.

In this work, three types of stable PdZn nanoparticles with different surface atomic architectures, namely PdZn_Disordered, PdZn_Ordered, and Pd@Zn_Core-shell (Pd: Zn = 1: 1), have been prepared to examine the surface structure effects toward ORR in alkaline medium. TEM, HAADF-STEM, HR-TEM, and XRD measurements revealed the amorphous PdZn, ordered PdZn, and ordered-Pd-core with disordered-Zn-shell structures for PdZn_Disordered, PdZn_Ordered, and Pd@Zn_Core-shell, respectively. The electrocatalytic performance followed the order of Pd@Zn_Core-shell > PdZn_Ordered » PdZn_Disordered, while Pd@Zn_Core-shell exhibited the best electrocatalytic ORR performance, even superior to the Pd/C and Pt/C catalysts.

2. Experimental section

2.1. Materials

Palladium acetate (Pd(OAc)$_2$, 99%), acetone (98%), and glycol ether (98%) were purchased from Energy Chemicals (Shanghai, China). Zinc acetate (Zn(OAc)$_2$, 99%) was obtained from Fuchen Chemical Reagents (Tianjin, China), sodium borohydride (NaBH$_4$, 98%), commercial Pd/C (20 wt% for Pd) and Pt/C (20 wt% for Pt) catalysts were purchased from Aladdin Chemical (Shanghai,

China). All the chemicals were used as received without further treatment.

2.2. Synthesis of PdZn_Disordered, PdZn_Ordered and Pd@Zn_Core-shell

Preparation of PdZn_Disordered: Disordered PdZn alloys were fabricated by following a previously documented protocol [38]. Typically, 0.2 mmol of palladium acetate were first dissolved into 10 mL of acetone by sonication, while 0.2 mmol of zinc acetate were dissolved into 50 mL of 2-ethoxyethanol under continuous stirring. Then, the above two solutions were mixed together under vigorous stirring for 10 min. Subsequently, a freshly prepared NaBH$_4$ aqueous solution (10 mL, 0.4 M) was added into the above solution at ambient temperature under stirring for 15 min. The solution immediately changed from yellow into brown black, indicating the formation of PdZn alloys. The final product obtained by filtration was washed with copious water ten times and ethanol twice and was dried under vacuum. It is denoted as PdZn_Disordered.

Preparation of PdZn_Ordered: After calcining the PdZn_Disordered sample under 0.1 MPa Ar/H$_2$ (10%) atmosphere at 600 °C for 5 h, with a heating rate of 1 °C min^{-1}, the product was collected and named as PdZn_Ordered.

Preparation of Pd@Zn_Core-shell: In a typical synthesis, 0.2 mmol of palladium acetate were first dissolved in a mixed solvent made of 10 mL of acetone and 50 mL of 2-ethoxy ethanol, and the solution was kept under stirring at 393 K for 30 min and cooled down to room temperature. Then, 10 mL of 0.02 M zinc acetate aqueous solution were added into the above mixture. Subsequently, 10 mL of freshly prepared 0.4 M NaBH$_4$ aqueous solution were added into the solution quickly. The formed black precipitates were collected by filtration, washed with plenty of water ten times and ethanol twice, and then dried in vacuum. The collected solid was the final product denoted as Pd@Zn_Core-shell.

2.3. Characterizations

The morphology and surface structural information were acquired using high angle annular dark-field (HAADF) scanning transmission electron microscopy (STEM, JEM-2100F) at an acceleration voltage of 200 kV. Energy dispersive X-ray (EDX) elemental mappings were recorded on a FEI Tecnai F20 machine. Powder X-ray diffraction patterns (XRD) were obtained on a Bruker D8 diffractometer with Cu K$_\alpha$ radiation (λ = 0.1541 nm). X-ray photoelectron spectroscopy (XPS) was conducted with an Escalab 250 photoelectron spectrometer (Thermo fisher scientific, USA).

2.4. Electrochemistry

Electrochemical measurements for ORR were performed using a CHI 750E workstation (CH Instruments Inc.) with a conventional three-electrode system in an O$_2$-saturated 0.1 M KOH solution at ambient temperature. The as-prepared catalyst-coated glassy carbon disk and gold ring were used as the working electrodes (S$_{disk}$ = 0.2475 cm^2). Ag/AgCl electrode (E_{RHE} = $E_{Ag/AgCl}$ + 0.059 × pH + 0.197, RHE = reversible hydrogen electrode) and a platinum foil (1.00 cm × 1.00 cm) were used as the reference and counter electrode, respectively. All potentials hereafter in the text are with reference to the RHE. Typically, 2 mg of each sample prepared as above were first dispersed in 1 mL of ethanol by sonication for at least 1 h to prepare a homogeneous catalyst ink. The Pd/C and Pt/C electrocatalysts were also prepared by the same method without adding additional carbon support. 20 μL of Nafion (5 wt%) were then added into the catalyst ink under sonication. Subsequently, 10 μL of the catalyst ink were dropwise cast onto the glassy carbon

electrode surface and dried at room temperature. The total catalyst loading was set as 80.8 μg cm^{-2} for all the samples [39–41]. For the Pd/C and Pt/C catalysts, the metal loading was 16.2 μg$_{metal}$ cm^{-2}. Prior to each electrochemical measurement, the catalyst on the glassy carbon electrode was electrochemically cleaned by potential cycles (−0.04 V to +1.16 V) of 10 min in a N$_2$-saturated alkaline solution. Subsequently, the activation of the catalyst was carried out in an O$_2$-saturated alkaline solution through potential cycles for 20 min within a potential range of − 0.04 V to +1.16 V. The cyclic voltammetric (CV) measurements were performed at a scan rate of 10 mV s^{-1} without rotating the working electrode. Linear sweep voltammetric (LSV) measurements were conducted at different rotation rates (400–2025 rpm) within the potential range from − 0.04 V to +1.16 V (vs. RHE) at the same scan rate of 10 mV s^{-1}. Chronoamperometric tests (i-t) were carried out in an O$_2$-saturated 0.1 M KOH solution at +0.5 V and 900 rpm for 30,000 s, while accelerated durability tests (ADTs) were performed by cycling the catalyst over the potential range of +0.6 V to +1.0 V at 100 mV s^{-1} [42–44]. The electrochemical active surface area (ECSA) of each catalyst was determined using the CO-stripping method in 0.1 M HClO$_4$. The total mass loading on the glass carbon electrode was 100 μg for all the samples. Firstly, 0.1 M HClO$_4$ electrolyte was saturated with N$_2$ for 20 min to remove the dissolved oxygen; subsequently, CO was bubbled to attain a full monolayer of absorbed CO on the metal surface under an applied potential of +0.05 V for 10 min. Following that, N$_2$ was bubbled for 5 min to remove CO in the electrolyte, while maintaining the potential of the working electrode at +0.05 V. Finally, CO-stripping and background CVs were recorded from 0.1 to 1.06 V vs. RHE at a scan rate of 10 mV s^{-1}. A saturated calomel electrode was employed as reference electrode ($E_{RHE} = E_{SCE} + 0.059 \times pH + 0.2415$) [45,46].

3. Results and discussions

Upon preparation of the samples, their chemical microstructure was first observed by SEM measurements. As shown in Fig. S1, all three samples exhibited granular structures, whereas the Pd@Zn_Core-shell sample showed well-defined spherical morphologies and PdZn_Ordered had more rough surfaces and blurred edges. TEM, HR-TEM and elemental mapping tests were then conducted (Fig. 1). Fig. 1a, e and i show typical TEM images of PdZn_Disordered, PdZn_Ordered, and Pd@Zn_Core-shell, respectively. Spherical particles were observed for all the samples. Compared with PdZn_Disordered and PdZn_Ordered, Pd@Zn_Core-shell showed unusual morphology, as there were several thin floccules partially covering on the surface of the particles with incomplete encirclement. The average diameters of the PdZn_Disordered, PdZn_Ordered, and Pd@Zn_Core-shell particles were calculated as 80.95 ± 2.54 nm, 87.81 ± 2.44 nm, and 90.15 ± 2.11 nm (core), respectively. It is noted that in view of the amorphous and irregular Zn shell, it is more reasonable to consider the core diameter as the size of the particle for Pd@Zn_Core-shell [47,48]. High-angle annular dark-field scanning transmission electron microscopic (HAADF-STEM) analysis was then conducted to further disclose the structural features and elemental distribution. The red marked square areas of Fig. 1b, f and j were the analytical regions of the HAADF-STEM images for PdZn_Disordered, PdZn_Ordered, and Pd@Zn_Core-shell, respectively. Green images (Fig. 1c, g and k) and red images (Fig. 1d, h and l) show the elemental distributions of Pd and Zn, respectively. For both PdZn_Disordered and PdZn_Ordered, Pd and Zn were well intermixed with good uniformity, suggesting formation of alloyed structures for both samples. Such conclusion can be further corroborated by the corresponding line-scan profiles depicted in Fig. 1m and n. The distribution trend of Pd almost overlapped with that of Zn, indicating both elements

were homogeneously scattered. However, for Pd@Zn_Core-shell, from the elemental mappings shown in Fig. 1k and l, one can notice that heavily dense Pd atoms were located at the core, while the concentration of Zn inside the core was much lower, but Zn had a somewhat partially denser distribution around the core. This suggests the formation of Pd@Zn core-shell structure, which was further confirmed by the line-scan profile illustrated in Fig. 1o. It can be noted that Pd exhibited a peak-shaped distribution with a high concentration in the middle, while Zn had an exceedingly lower concentration in the middle but slightly enriched at the edges. The combined elemental mapping results with the line-scan profile observations offer solid evidences for successful formation of Pd@Zn core-shell structure.

To further closely scrutinize the surface atomic arrangement, high-resolution transmission electron microscopy (HR-TEM) was next conducted for the PdZn_Ordered and Pd@Zn_Core-shell samples. As shown in Fig. 2a and b, well-defined lattice fringes can be clearly identified for both samples. For PdZn_Ordered, the lattice fringes with interplanar distances of 0.121 nm, 0.205 nm, 0.219 nm, and 0.290 nm are in good agreement with PdZn (3 1 1), PdZn(2 0 0), PdZn(1 1 1), and PdZn(1 1 0) crystal planes [49]. For Pd@Zn_Core-shell, the interplanar distances of 0.138 nm, 0.195 nm, and 0.225 nm correspond well with Pd (2 2 0), Pd(2 0 0), and Pd(1 1 1) crystal planes, respectively [50,51]. It is noteworthy that the crystal plane associated with zinc was not detected, indicating that Zn possessed a disordered or amorphous structure in the shell of the Pd@Zn core-shell. In addition, energy dispersive X-ray (EDX) spectroscopy on SEM was performed to estimate the atomic percentages of all elements in the three samples. A monocrystalline silicon plate was employed as carrier to avoid interference of other elements, especially carbon. As depicted in Fig. S2, Pd, Zn, C and O were all present in the three samples. From EDX analysis (Table S1), the atomic percentages of Zn and Pd were similar for all three samples, which was consistent with the nominal ratio in the synthetic process (atomic ratio Pd: Zn = 1: 1). One may notice that the weight percentages of Pd and Zn in PdZn_Ordered were slightly higher than that in PdZn_Disordered, reminiscent of the calcination process for preparing PdZn_Ordered from PdZn_Disordered, as a small amount of C was probably lost during this process. In the three samples carbon mainly originated from the precursor compound, while oxygen should be from the carbon matrix and/or metal oxides. The catalytic activity of carbon for ORR is much lower than that of precious metal Pd, that is, the residual carbon had presumably little influence on the catalytic property of the samples. Previous studies have shown that only carbon materials doped with heteroatoms may have a remarkable catalytic activity for ORR [52]. To verify the results from EDX, inductively coupled plasma-mass spectrometry (ICP-MS) was also conducted, and the corresponding results are summarized in Table S1. The metal mass content obtained from ICP-MS was in good agreement with EDX. The weight percentages of Pd for PdZn_Disordered, PdZn_Ordered, and Pd@Zn_Core-shell were 44.04 wt%, 58.96 wt%, and 42.35 wt%, respectively. The ICP-MS results also provided a reference for the subsequent calculation of electrochemically active surface area (ECSA) and mass activity (MA).

The crystal structure of the samples was revealed by XRD measurements, as shown in Fig. 2c. For PdZn_Disordered, there are two broad peaks with extremely weak signal (2θ = 40.03° and 46.65°), coinciding with the diffraction peak of Pd fcc facet (PDF#46-1043) [38]. This implies that only very few of the palladium atoms had an ordered structure and that most of them exhibited amorphous and disordered architectures. Moreover, the signal from Zn can be barely identified, probably covered by the signal from Pd. These observations attest that PdZn_Disordered can be defined as an amorphous bimetallic alloyed material. In contrast, sharp peaks
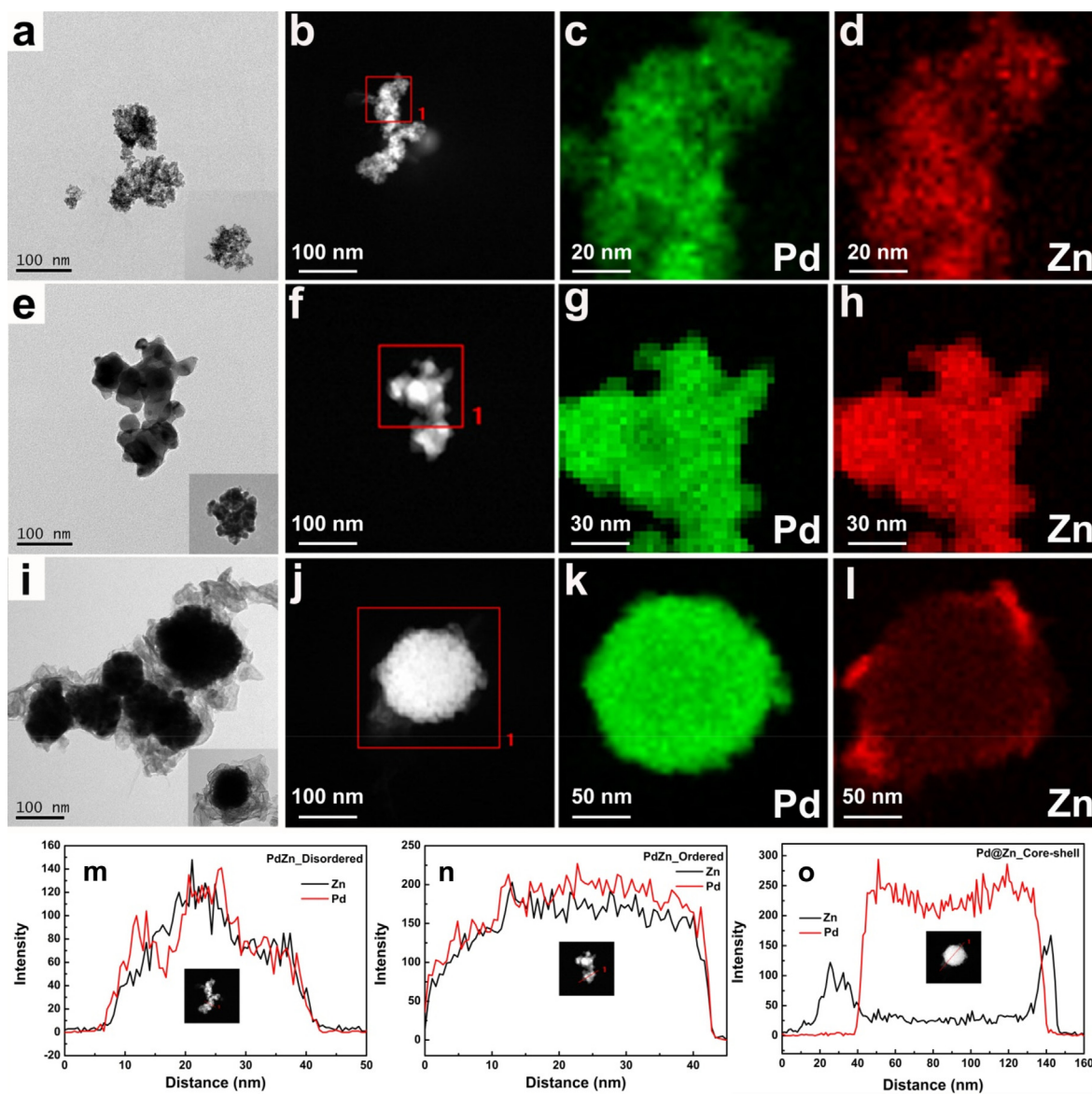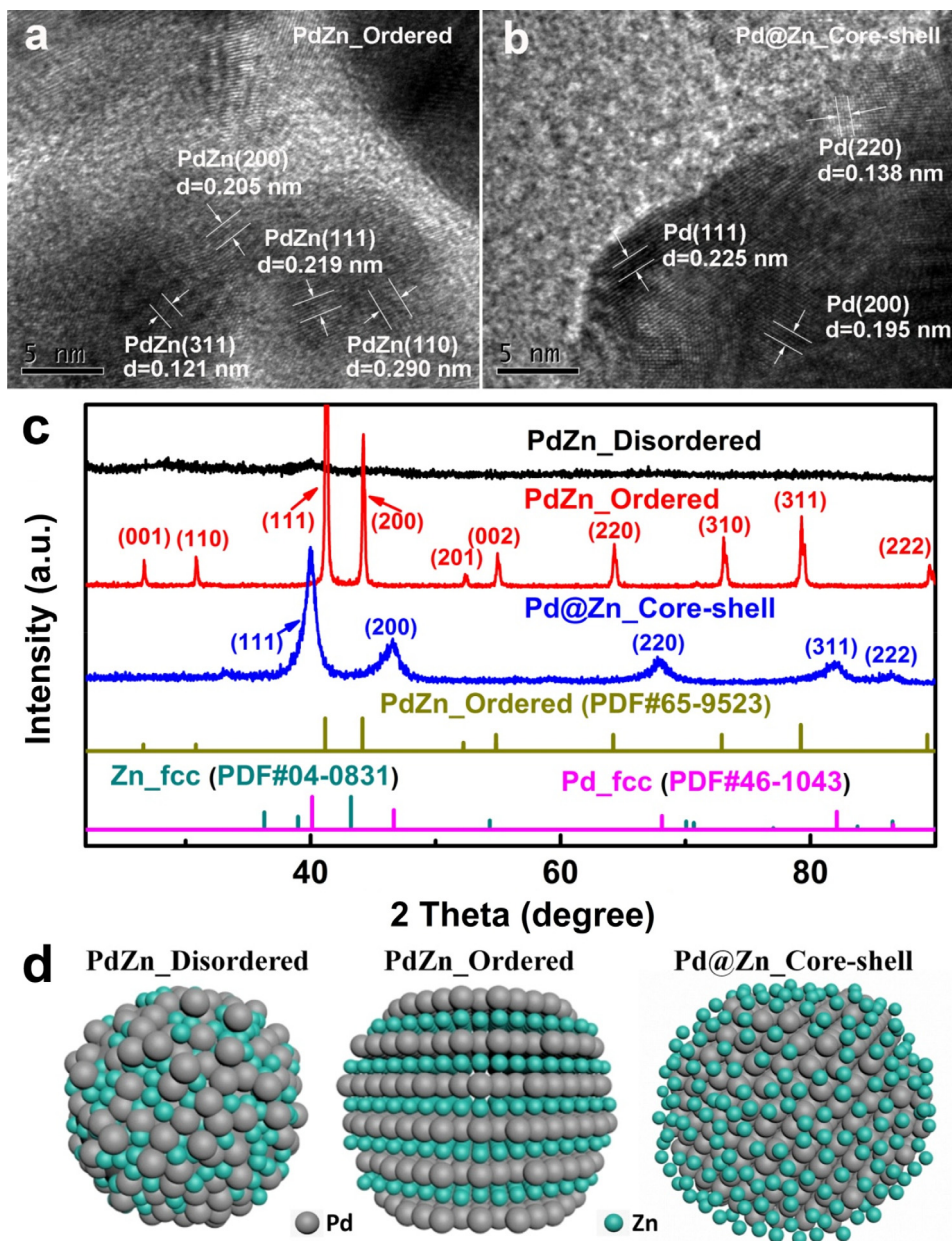
Fig. 1. Representative TEM images of (a) PdZn_Disordered, (e) PdZn_Ordered, and (i) Pd@Zn_Core-shell. Typical HAADF-STEM image of (b) PdZn_Disordered and (c-d) the corresponding elemental mappings (Pd and Zn). Typical HAADF-STEM image of (f) PdZn_Ordered and (g-h) the corresponding elemental mappings (Pd and Zn). Typical HAADF-STEM image of (j) Pd@Zn_Core-shell and (k-l) the corresponding elemental mappings (Pd and Zn). Line-scan profiles of Zn and Pd in PdZn_Disordered (m), PdZn_Ordered (n), and Pd@Zn_Core-shell (o) from the direction marked by a red line in the corresponding inserted images.

with strong signal can be readily identified for the PdZn_Ordered and Pd@Zn_Core-shell samples. It is noteworthy that the 2θ peaks located at 26.62°, 30.82°, 41.17°, 44.14°, 52.29°, 54.83°, 64.20°, 72.90°, 79.23° and 89.35° in the PdZn_Ordered sample correspond well with previously documented signal for PdZn intermetallic alloy compounds (PDF#65-9523) [53,54], confirming the successful acquirement of ordered structure. As for Pd@Zn_Core-shell with core-shell structure, the diffraction peaks are in good accordance with the single crystal diffraction peaks of palladium (PDF#46-1043) [38,55,56]. There are five apparent peaks at 40.12°, 46.66°, 68.12°, 82.10°, and 86.62°, which can be attributed to the (1 1 1), (2 0 0), (2 2 0), (3 1 1), and (2 2 2) crystalline planes of metallic Pd, respectively. It can be concluded that the palladium core adopted an ordered crystal structure. Interestingly, there is no peak corresponding to metallic Zn in Pd@Zn_Core-shell, further confirming that the zinc shell in the periphery had a disordered structure. Based on the above analysis, the Pd@Zn_Core-shell sample can be defined as a Pd-core-ordered and Zn-shell-disordered bimetallic composite.

Based on the combined analyses of STEM, HR-TEM, and XRD results, the surface structure of the three samples are clearly expressed. For a more intuitive understanding and comparison, structural models of the samples are shown in Fig. 2d, where disordered and ordered palladium-zinc alloy structures can be easily observed for PdZn_Disordered and PdZn_Ordered. For Pd@Zn_Core-shell, the ordered structure of the Pd core and the disordered structure of the Zn shell were directly displayed. Furthermore, by correlating the crystal structure from the XRD analysis, the crystal models of PdZn_Ordered and the core of Pd@Zn_Core-shell were simulated and are shown in Fig. S3. Well-defined tetragonal and face-centered cubic (fcc) skeletons can be observed for PdZn_Ordered and for the core of Pd@Zn_Core-shell, respectively.

X-ray photoelectron spectroscopy (XPS) was next conducted to obtain insight into the chemical compositions and valence states of the catalysts. The survey-scan XPS spectra shown in Fig. S4 attested the presence of C, O, Pd and Zn in all three samples. From XPS, the surface atomic percentages of Zn and Pd were estimated as 6.41 at.% and 5.44 at.% for PdZn_Disordered, 7.24 at.% and 6.01

Fig. 2. Representative HR-TEM images of (a) PdZn_Ordered and (b) Pd@Zn_Core-shell. Some relatively obvious lattice fringes and their spacings are marked in the figure. (c) XRD patterns of PdZn_Disordered, PdZn_Ordered and Pd@Zn_Core-shell. (d) Structure models of PdZn_Disordered, PdZn_Ordered and Pd@Zn_Core-shell.

at.% for PdZn_Ordered, and 13.69 at.% and 2.42 at.% for Pd@Zn_Core-shell, respectively. In terms of the first two alloy samples, the surface atomic ratios of Pd and Zn are close to 1: 1, which is in accord with the nominal ratio. It can be noted that Pd@Zn_Core-shell exhibited a higher Zn content than the other two alloy samples, indicating that zinc is mainly distributed in the outer layer shell, which is consistent with the previous HAADF-STEM analysis. The corresponding weight percentages for the four main elements (C, O, Zn and Pd) from XPS, EDS and ICP-MS are summarized in Table S1. One may notice that XPS showed higher C and O contents than EDX. This excess carbon and oxygen are probably derived from the interference of the conductive adhesive. In addition, compared with the disordered and ordered samples, the Core-shell sample exhibited a higher Zn content in XPS rather than that in EDX. This is probably due to the fact that XPS is a surface analysis technique with a few nanometer detection depth, hence the outer layer Zn can be more easily detected.

The XPS core-level spectra of the Pd 3d electrons in PdZn_Disordered, PdZn_Ordered, and Pd@Zn_Core-shell are presented in Fig. 3a. For PdZn_Disordered and PdZn_Ordered, the binding energies of the Pd $3d_{3/2}$ and Pd $3d_{5/2}$ electrons were nearly identical, approximately at 341.0 eV and 335.8 eV respectively. For Pd@Zn_Core-shell, the binding energies of the Pd $3d_{3/2}$ and Pd $3d_{5/2}$ electrons (340.2 eV and 334.9 eV) were smaller than that of PdZn_Disordered and PdZn_Ordered, suggesting a higher amount of Pd(0) in the sample. The two peaks for the Pd $3d_{3/2}$ and Pd $3d_{5/2}$ electrons could be deconvoluted into two pairs of doublets. The two peaks at high binding energy of 341.1 eV and 335.8 eV were assigned to Pd(II) species, while the other two peaks at low binding energy of 340.2 eV and 334.9 eV were consistent with metallic Pd [57–60]. The percentages of Pd(0) in PdZn_Disordered, PdZn_Ordered, and Pd@Zn_Core-shell were calculated as 8.5%, 24.8%, and 67.8%, respectively. Compared with PdZn_Disordered, PdZn_Ordered exhibited a higher Pd(0) content, probably due to
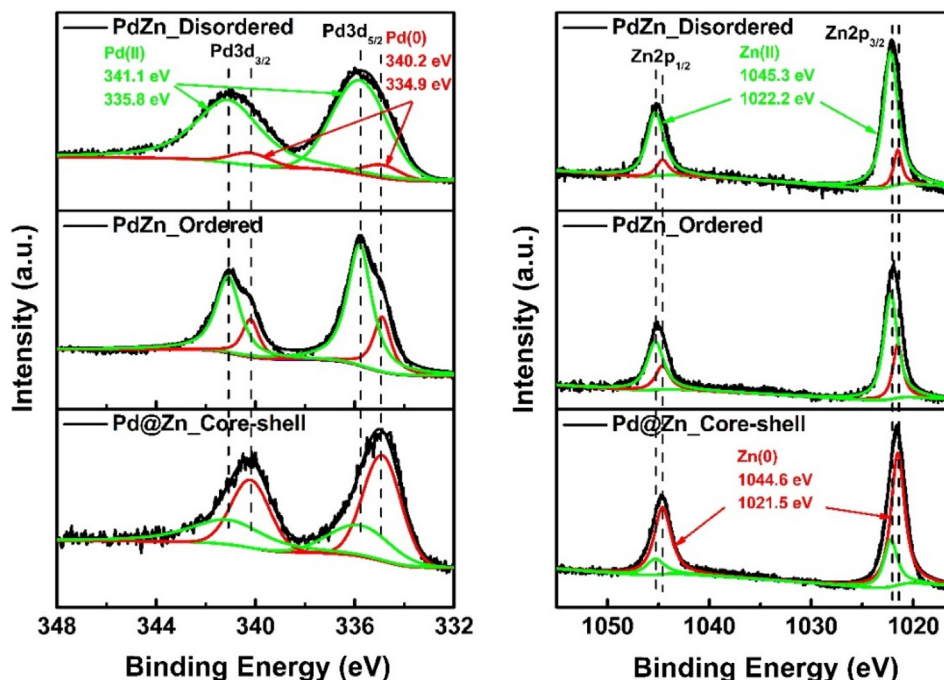
Fig. 3. XPS core-level spectra of the (a) Pd 3d electrons and (b) Zn 2p electrons in PdZn_Disordered, PdZn_Ordered and Pd@Zn_Core-shell.

that part of the palladium were reduced during the calcination process under reductive atmospheric environment (Ar/H_2). For Pd@Zn_Core-shell, the highest percentage of metallic Pd was obtained, presumably due to that the outer transition metal layer could protect the palladium core from being oxidized by air [61]. Fig. 3b shows the high-resolution XPS spectra for the Zn 2p electrons. PdZn_Disordered and PdZn_Ordered exhibited almost identical binding energies for the Zn 2p electrons, while slightly lower values can be observed for Pd@Zn_Core-shell, indicating a higher amount of low valent zinc element. The two peaks from the Zn $2p_{1/2}$ and Zn $2p_{3/2}$ electrons could be deconvoluted into a pair of two subpeaks. The two green peaks (1045.3 eV and 1022.2 eV) could be ascribed to Zn(II), while the two red peaks (1044.6 eV and 1021.5 eV) were assigned to Zn(0) species [62,63]. The Zn(0) contents of the three samples followed the order: Pd@Zn_Core-shell (74.3%) > PdZn_Ordered (26.9%) > PdZn_ Disordered (12.4%). The results indicate that there is strong electronic interaction between the Pd core and the Zn shell for Pd@Zn_Core-shell. Such interaction may play an important role in the electrocatalytic reaction by adjusting the adsorption energy of the oxygenated intermediates [64–66]. The XPS core-level spectra for the C 1s and O 1s electrons in the three samples can be found in Fig. S5, further attesting that oxygen are not only from the metal oxides, but also from the carbon substrates being in the form of C—O and O—C═O, which agrees well with the results presented in Fig. 3 and Table S1.

Subsequently, the electrocatalytic performance toward ORR of PdZn_Disordered, PdZn_Ordered, and Pd@Zn_Core-shell was examined and compared with that of Pd/C and Pt/C. The ORR catalytic results are summarized in Table 1. As illustrated in the cyclic voltammograms in Fig. 4a, a sharp peak at around 0.7 V − 0.85 V attributed to the reduction of oxygen can be found for all the samples, implying effective activity. The cathodic peak potential follows the order of Core-shell > Ordered > Disordered. Pd@Zn_Core-shell not only exhibited the highest cathodic peak potential, but also the largest cathodic peak current density, indicating a superior ORR performance. Fig. 4b depicts the RRDE voltagramms in O_2-saturated 0.1 M KOH solution at 1600 rpm, from which the onset potentials, half wave potentials and diffusion-

limited current densities can be determined. The polarization curve can be roughly divided into three sections, namely the kinetics-controlled section, the mixed kinetics/diffusion-controlled section, and the diffusion-controlled section. The potential corresponding to the boundary between the kinetics-controlled section and the mixed kinetics/diffusion-controlled section is the onset potential, which is the starting potential at which the current begins to rapidly increase. The half wave potential is close to the middle of the mixed kinetics/diffusion-controlled section. The limiting current corresponds to the current in the diffusion-controlled section, which generally has reached a plateau. As the rotation speed increases, the onset potential and the half-wave potential remain almost unchanged, while the limiting current density increases. Pd@Zn_Core-shell exhibited the highest onset potential (0.98 V), the highest half-wave potential (0.82 V) and the largest diffusion-limited current density (−6.07 mA·cm^{-2}) among the three samples. Its diffusion-limited current density was much higher than that of Pd/C and Pt/C, whereas its onset potential value was higher than that of Pd/C and comparable with that of Pt/C. The results indicate that it has superior activity to the benchmark Pd/C and Pt/C catalysts for ORR electrocatalysis in alkaline media. As summarized in Table 1, the onset potential, half-wave potential, Tafel slope b, ECSA, SA, MA, and TOF followed the above-mentioned cathodic peak potential trend, showing an ORR performance order of Pd@Zn_Core-shell > PdZn_Ordered > PdZn_ Disordered. This suggests that Pd@Zn_Core-shell possessed the highest intrinsic activity. The related formulas for calculating ECSA, SA, MA, and TOF can be found in the Supplementary Material.

Based on the RRDE measurements (Fig. 4b), the electron transfer number(n) and the H_2O_2 yield in ORR (Fig. 4c) can be quantified by

$$n = \frac{4I_D}{I_D + I_R/N} \quad (1)$$

and

$$H_2O_2\% = \frac{200I_R/N}{I_D + I_R/N} \quad (2)$$

Table 1
The ORR performance summary of PdZn_Disordered, PdZn_Ordered, Pd@Zn_Core-shell, Pd/C, and Pt/C including onset potential (E_{onset}), half wave potential ($E_{1/2}$) at 1600 rpm, Tafel slope b (mV dec^{-1}), electrochemically active surface area (ECSA), specific activity (SA), mass activity (MA) at 0.85 V, and turnover frequency (TOF) at 0.85 V (The tests were conducted in 0.1 M KOH).

Samples	E_{onset} (V)	$E_{1/2}$ (V)	Tafel slope b(mV dec^{-1})	ECSA(m^2/g$_{Pd\ or\ Pt}$)	SA(μA/cm$^2_{Pd\ or\ Pt}$)	MA(mA/mg$_{Pd\ or\ Pt}$)	TOF(s^{-1})
PdZn_Disordered	0.93	0.74	81.3	48.20	17.36	8.37	0.0032
PdZn_Ordered	0.97	0.81	59.8	55.04	44.41	24.44	0.0073
Pd@Zn_Core-shell	0.98	0.82	58.0	90.22	48.83	44.05	0.0135
Pd/C	0.95	0.76	89.2	103.77	37.68	39.10	0.0126
Pt/C	0.98	0.80	78.9	198.81	34.18	67.95	0.0377
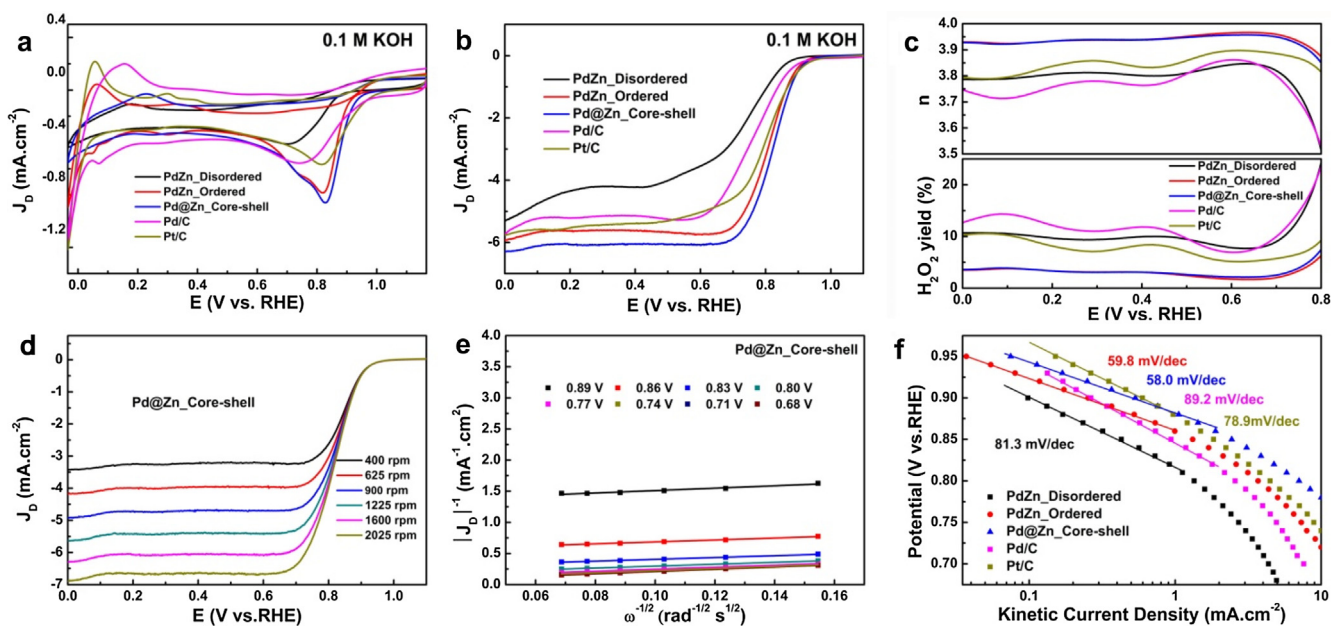
Fig. 4. (a) Cyclic and (b) RRDE voltammograms of a glassy carbon electrode with deposited PdZn_Disordered, PdZn_Ordered, Pd@Zn_Core-shell, Pd/C, and Pt/C obtained in O$_2$-saturated 0.1 M KOH solution at 1600 rpm scanning the potential from 1.166 V to 0.034 V. (c) Plots of H$_2$O$_2$ yield and electron transfer number (n) of a glassy carbon electrode with deposited PdZn_Disordered, PdZn_Ordered, Pd@Zn_Core-shell, Pd/C, and Pt/C. (d) RRDE voltammograms for Pd@Zn_Core-shell obtained at rotation rates of 400 to 2025 rpm. (e) The corresponding Koutecky-Levich (K-L) plots for Pd@Zn_Core-shell at different electrode potentials from 0.68 V to 0.89 V. (f) The corresponding Tafel plots for Pd@Zn_Core-shell, Pd/C, and Pt/C. All measurements were conducted at a catalyst loading of 80.8 μg cm^{-2} in an O$_2$-saturated 0.1 M KOH aqueous solution at a potential scan rate of 10 mV s^{-1}.

where I_D is the disk current density, I_R is the ring current density, and N is the RRDE collection efficiency with a value of 0.37 (given by the RRDE manufacturer). Within the potential range of 0 V to +0.70 V, the electron transfer number (n) values were 3.79–3.85, 3.92–3.96, 3.92–3.95, 3.71–3.86, and 3.79–3.90 for PdZn_Disordered, PdZn_Ordered, Pd@Zn_Core-shell, Pd/C, and Pt/C, respectively. The electron transfer numbers for the PdZn_Ordered and Pd@Zn_Core-shell samples were higher than those for the PdZn_Disordered, Pd/C, and even Pt/C. Also, their values are quite close to 4, suggesting that the ORR process proceeded overwhelmingly adopts a 4-electron transfer pathway for both samples. Correspondingly, the H$_2$O$_2$ yields for the two samples remained at a very small value of less than 3% within the potential range from +0.0 V to +0.7 V, also much lower than that for PdZn_Disordered, Pd/C, and Pt/C (Fig. 4c). The results imply that a negligible amount of H$_2$O$_2$ as byproduct was produced during the ORR process for both PdZn_Ordered and Pd@Zn_Core-shell. Above ca. 0.7 V, I_D decreased dramatically, I_R also decreased slightly, and as the decrease of I_R was much less than that of I_D, the I_R/I_D value became larger, which resulted in decrease of the electron transfer number ($n = \frac{4I_D}{I_D+I_R/N} = \frac{4}{1+I_R/(I_DN)}$).

Fig. 4d depicts RRDE measurements at various rotation rates ranging from 400 rpm to 2025 rpm for Pd@Zn_Core-shell. It can be noticed that the absolute value of the current density grew evenly with increasing rotation rate. The corresponding K-L plots based on the polarization curves are shown in Fig. 4e. It can be found that, in the potential range from 0.68 V to 0.89 V, the Koutecky–Levich (K-L) plots of Pd@Zn_Core-shell are largely linear with very consistent slopes, suggesting a first-order reaction kinetics with regard to dissolved oxygen concentration in the solution [67,68]. For comparison, the LSV curves and corresponding K-L plots of the other samples as well as for Pd@Zn_Core-shell are shown in Fig. S6, where a similar current change trend with excellent linearity is observed for all the five samples (0.68 V to 0.86 V).

The electron-transfer kinetics can be further analyzed by using the Koutecky–Levich (K–L) approach [69–71]. As the voltammetric disk current (I_D) includes both kinetic (I_k) and diffusion-controlled (I_d) contributions, the K–L equation can be expressed as shown in Eqs. (3) and (4):

$$\frac{1}{I_D} = \frac{1}{I_k} + \frac{1}{I_d} = \frac{1}{I_k} + \frac{1}{B\omega^{1/2}} \qquad (3)$$

$$B = 0.62nFAC_oD_o^{2/3}\nu^{-1/6} \qquad (4)$$

where ω is the electrode rotation rate, n is electron-transfer number, F is the Faraday constant (96485C mol^{-1}), A is the geometric surface area of the electrode, C_0 is the oxygen concentration in O$_2$-saturated solution (1.26 $\times$ 10^{-6} mol cm^{-3}), D_0 is the diffusion

coefficient of O_2 in 0.1 M KOH aqueous solution (1.93×10^{-5} cm^2 s^{-1}), v is the solution kinematic viscosity (0.01 cm^2 s^{-1}), and k is the electron-transfer rate constant [72]. The K-L plots exhibited good linearity, which indicated that the electron transfer numbers can be determined from the slopes of the K-L plots (Fig. S6). Through Eq. (4), the corresponding electron transfer numbers within the mixed kinetics/diffusion-controlled section (0.68 V to 0.86 V) were calculated as 2.55–3.79, 2.89–3.93, 3.59–3.94, 2.84–3.82 and 3.27–3.88 for PdZn_Disordered, PdZn_Ordered, Pd@Zn_Core-shell, Pd/C, and Pt/C, which is consistent with the variation trend of electron transfer numbers at high potential in Fig. 4c.

To further unravel the reaction kinetics for Pd@Zn_Core-shell, the Tafel slope was extrapolated and compared with that of PdZn_Disordered, PdZn_Ordered, Pd/C, and Pt/C, as shown in Fig. 4f. The related values were calculated by using the kinetic current density values obtained by the intercept of the y-axis in the K-L plots. Two well-defined linear regions can be found in the mixed kinetics/diffusion-controlled section between the logarithm of the absolute value of the kinetic current density and the potential for all five catalysts. Compared with region 1 (high potential), region 2 (low potential) had a larger Tafel slope. The change of Tafel slope is closely related to kinetic mechanism for ORR, and is due to different adsorption and rate-determining steps [70,73]. Here, we compared the Tafel slopes in region 1 to investigate whether the first electron transfer to the oxygen molecule is the ORR rate determining step. Pd@Zn_Core-shell displayed a Tafel slope of 58.0 mV dec^{-1}, lower than that for PdZn_Disordered (81.3 mV dec^{-1}) and for PdZn_Ordered (59.8 mV dec^{-1}), even lower than that for Pd/C (89.2 mV dec^{-1}) and Pt/C (78.9 mV dec^{-1}), which further attests its superior electrocatalytic activity and the fastest reaction kinetics. Note that the Tafel slope value for Pd@Zn_Core-shell was slightly smaller but close to 60 mV dec^{-1}, which suggests that the ORR rate determining step is probably the first electron transfer to oxygen molecules during the electrocatalytic process [57,58,67,74]. One phenomenon that could not be ignored was that the Tafel curves of Pd@Zn_Core-shell and Pt/C intersected at a potential of 0.89 V. Pt/C exhibited slightly better performance than Pd@Zn_Core-shell above 0.89 V, which is the starting point of the mixed kinetics/diffusion-controlled section. However, Pd@Zn_Core-shell had the same onset potential with Pt/C, and more intriguingly, once the potential was lower than 0.89 V, Pd@Zn_Core-shell demonstrated better kinetic activity and could achieve faster four-electron transfer than Pt/C.

To further disclose the physical origin of the differences in intrinsic ORR activity, ECSA measurement was conducted (Fig. S7). The ECSA values of the catalysts were calculated and are summarized in Table 1. It can be noted that Pd@Zn_Core-shell had a much higher ECSA than PdZn_Ordered and PdZn_Disordered, which was probably responsible for its superior ORR activity. As the outer layer, the porous flocculation structure of the Zn shell in Pd@Zn_Core-shell can fully expose the active sites of Pd to maximize the catalytic activity. Based on ECSA, the corresponding SA values were estimated by the related formula mentioned in Supplementary Material. As shown in Table 1, Pd@Zn_Core-shell exhibited the highest SA value (48.83 μA cm$_{Pd}^{-2}$), even larger than the Pd/C and Pt/C catalysts, which is an indicative of its superior intrinsic activity for ORR. In addition, MA values were compared to confirm the intrinsic activity of palladium. A similar order was demonstrated, where Pd@Zn_Core-shell displayed larger MA than PdZn_Disordered, PdZn_Ordered, and Pd/C. The TOFs for ORR were further calculated by the mass activity at 0.85 V [73,75]. As summarized in Table 1, the highest value of TOF among the three samples was found for Pd@Zn_Core-shell. The results illustrate that Pd@Zn_Core-shell exhibited the best intrinsic activity for ORR, superior to that for Pd/C.

Finally, the long-term stability for ORR of PdZn_Disordered, PdZn_Ordered, and Pd@Zn_Core-shell was assessed and compared with the Pd/C and Pt/C catalysts. The chronoamperometric response measurements were first recorded in an O_2-saturated 0.1 M KOH solution at +0.5 V and 900 rpm for 30,000 s. As depicted in Fig. 5a, after continuous operation of about 8 h, the current dropped to 78.30%, 91.58%, 94.30%, 78.82%, and 68.88% of its initial value for PdZn_Disordered, PdZn_Ordered, Pd@Zn_Core-shell, Pd/C, and Pt/C, respectively. PdZn_Ordered and Pd@Zn_Core-shell demonstrated higher long-term stability than PdZn_Disordered, Pd/C and Pt/C catalysts. Pd@Zn_Core-shell exhibited the best performance among the series catalysts. Furthermore, accelerated durability tests (ADT) of Pd@Zn_Core-shell were carried out by cycling the catalyst for 2500 cycles over the potential range from +0.6 V to +1.0 V at 100 mV s^{-1} in an oxygen-saturated 0.1 M KOH solution to further compare its stability with Pd/C and Pt/C. The half-wave potential shifts for Pd@Zn_Core-shell, Pd/C and Pt/C after 2500 cycles are shown in Fig. 5b, c and d. For Pd/C and Pt/C, the potentials shifted negatively by about ~38 mV and ~16 mV, respectively, while in sharp contrast, Pd@Zn_Core-shell shifted by only ~12 mV. The electron transfer numbers were reduced to 3.90–3.93, 3.64–3.83, and 3.77–3.85 within the potential range from 0 V to +0.70 V for Pd@Zn_Core-shell, Pd/C, and Pt/C, respectively. The above results from both i-t and ADT measurements imply that Pd@Zn_Core-shell possessed markedly superior long-term durability to the Pd/C and Pt/C catalysts.

Impressively, the ORR performance of Pd@Zn_Core-shell is superior to or at least comparable with the most recently reported PdM-based (M = transition metal) catalysts under the same electrochemical test conditions. The comparison results are summarized in Table S2. For instance, in 0.1 M KOH, the onset potential of Pd@Zn_Core-shell was 0.980 V, comparable with that of $Cu_{10}Pd$ [76], PdNi-NS/C [77], and Ni@Pd$_3$ [78], and superior to that of G-Cu$_3$Pd NCPs [20], PdFe/C-BAE [79], Co@Pd NC [39], and PdNi/NG [65]. It also exhibited a larger diffusion-limited current density of 6.07 mA cm^{-2} at 0.5 V, outperforming the G-Cu$_3$Pd NCPs [20], PdFe/C-BAE [79], PdNi-NS/C [77], Ni@Pd$_3$ [78], and PdNi/NG [65] catalysts.

The ORR activity and stability follows the order Pd@Zn_Core-shell > PdZn_Ordered » PdZn_Disordered, with Pd@Zn_Core-shell demonstrating the best performance. This can be mainly attributed to the different surface atomic arrangements. Firstly, from the structural perspective, well-defined core-shell structure and ordered structure can provide more predictable control over geometric and structural effects for catalysis optimization (e. g. new active sites might be generated), which cannot be afforded by the disordered structure [80]. Compared to PdZn_Disordered, the more uniform and ordered distribution of Pd atoms in PdZn_Ordered and Pd@Zn_Core-shell can lead to higher coordination and utilization of the Pd atoms, which is more favorable for the adsorption, activation, and dissociation of the oxygen molecules. This is why significantly higher activity was obtained for Pd@Zn_Core-shell and PdZn_Ordered than PdZn_Disordered [80,81]. Secondly, as evidenced by the XPS binding energy shift, stronger electronic interaction exists in Pd@Zn_Core-shell over PdZn_Ordered and over PdZn_Disordered. Such electronic interaction could make the d-band center of Pd downshift, weakening the adsorption of the oxygenated intermediates, and eventually leading to enhanced ORR performance [82–84]. Finally, as observed in the TEM study (Fig. 1i), the flocculated and disordered zinc shell incompletely surrounded the periphery of the Pd core in the Pd@Zn_Core-shell sample, which rendered some Pd atoms exposed as active sites for ORR. In addition, the zinc shell can prevent the palladium core from being oxidized by air, which probably contributed significantly to the robust stability of the Pd@Zn_Core-shell sample [61,84].
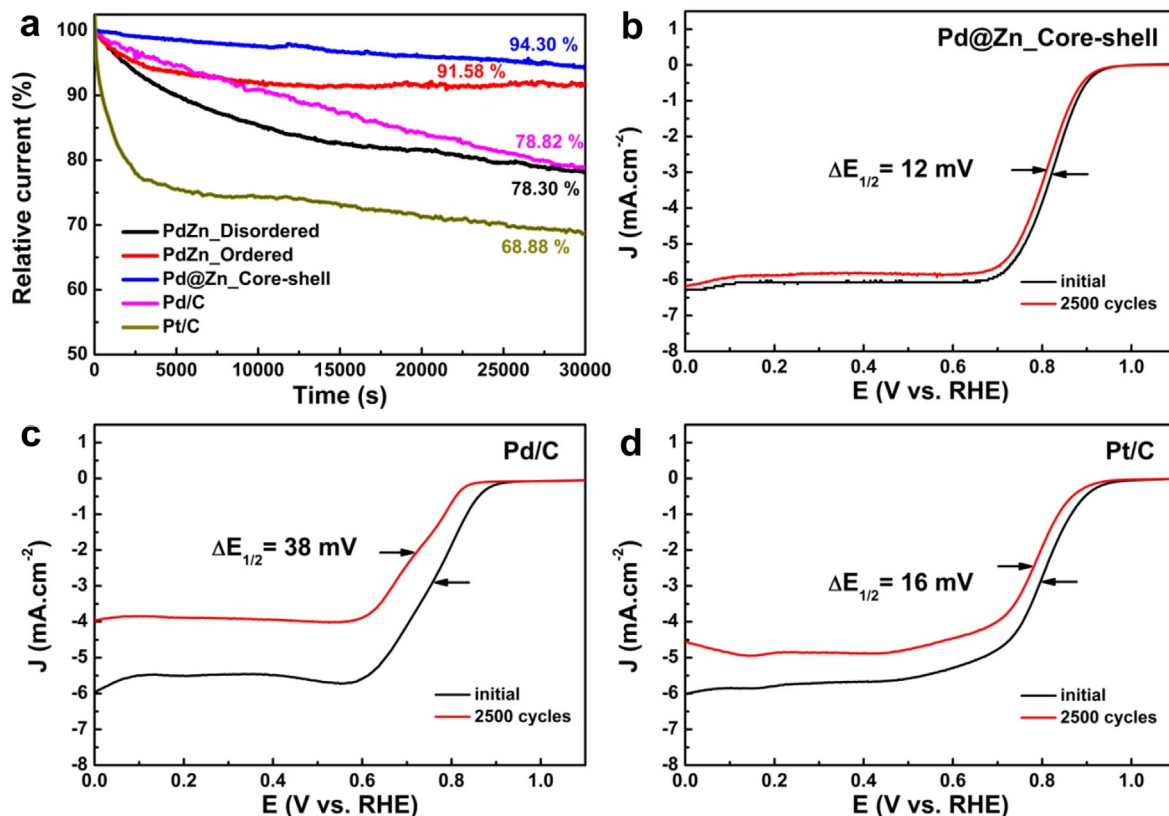
Fig. 5. (a) Chronoamperometric responses for ORR at Pd@Zn_Core-shell, Pd/C and Pt/C modified electrodes in an O$_2$-saturated 0.1 M KOH solution at +0.5 V and 900 rpm for 30, 000 s. The accelerated durability tests (ADT) of Pd@Zn_Core-shell (b), Pd/C (c) and Pt/C (d) were carried out before and after 2, 500 cycles between 0 and +1.1 V at a scan rate of 100 mV s^{-1} in an O$_2$-saturated 0.1 M KOH solution.

4. Conclusions

In conclusion, PdZn_Disordered, PdZn_Ordered and Pd@Zn_Core-shell (Pd: Zn = 1: 1) with three different surface structures have been successfully prepared and employed for ORR electrocatalysis in alkaline medium. Their structural architectures along with different surface atomic arrangements were observed and confirmed by multiple techniques, in conjunction with preliminary simulation of crystal models. Pd@Zn_Core-shell exhibited the best ORR performance in terms of onset potential, half-wave potential, diffusion-limited current and long-term durability, superior to Pd/C and Pt/C catalysts. The ORR performance followed the trend of Pd@Zn_Core-shell > PdZn_Ordered » PdZn_Disordered. A correlation between the electrocatalytic performance and the atomic surface structure of the catalyst has been successfully established. The study further underscores the importance of understanding the catalytic behaviors at the atomic level, and could shed light on designing efficient, durable and cost-effective non-platinum catalysts toward fuel cells applications and beyond.

Declaration of Competing Interest

The authors declare that they have no known competing financial interests or personal relationships that could have appeared to influence the work reported in this paper.

Acknowledgements

Appendix A. Supplementary material

Supplementary data to this article can be found online at https://doi.org/10.1016/j.jcat.2019.12.018.

References

[1] M. Winter, R.J. Brodd, What are batteries, fuel cells, and supercapacitors?, Chem. Rev. 104 (2004) 4245–4270.
[2] M.K. Debe, Electrocatalyst approaches and challenges for automotive fuel cells, Nature 486 (2012) 43–51.
[3] M. Liu, R. Zhang, W. Chen, Graphene-supported nanoelectrocatalysts for fuel cells: synthesis, properties, and applications, Chem. Rev. 114 (2014) 5117–5160.
[4] J. Wu, H. Yang, Platinum-based oxygen reduction electrocatalysts, Acc. Chem. Res. 46 (2013) 1848–1857.
[5] Z. Xia, L. An, P. Chen, D. Xia, Non-Pt nanostructured catalysts for oxygen reduction reaction: synthesis, catalytic activity and its key factors, Adv. Energy Mater. 6 (2016) 1600458.
[6] C.R. Raj, A. Samanta, S.H. Noh, S. Mondal, T. Okajima, T. Ohsaka, Emerging new generation electrocatalysts for the oxygen reduction reaction, J. Mater. Chem. A 4 (2016) 11156–11178.
[7] X. Huang, Z. Zhao, L. Cao, Y. Chen, E. Zhu, Z. Lin, M. Li, A. Yan, A. Zettl, Y.M. Wang, X. Duan, T. Mueller, Y. Huang, High-performance transition metal–doped Pt$_3$Ni octahedra for oxygen reduction reaction, Science 348 (2015) 1230–1234.
[8] L. Bu, N. Zhang, S. Guo, X. Zhang, J. Li, J. Yao, T. Wu, G. Lu, J.-Y. Ma, D. Su, X. Huang, Biaxially strained PtPb/Pt core/shell nanoplate boosts oxygen reduction catalysis, Science 354 (2016) 1410–1414.

[9] L. Wang, Z. Tang, W. Yan, Q. Wang, H. Yang, S. Chen, Co@Pt Core@Shell nanoparticles encapsulated in porous carbon derived from zeolitic imidazolate framework 67 for oxygen electroreduction in alkaline media, J. Power Sources 343 (2017) 458–466.

[10] G.-R. Xu, B. Wang, J.-Y. Zhu, F.-Y. Liu, Y. Chen, J.-H. Zeng, J.-X. Jiang, Z.-H. Liu, Y.-W. Tang, J.-M. Lee, Morphological and interfacial control of platinum nanostructures for electrocatalytic oxygen reduction, ACS Catal. 6 (2016) 5260–5267.

[11] G. Wu, J. Wang, W. Ding, Y. Nie, L. Li, X. Qi, S. Chen, Z. Wei, A strategy to promote the electrocatalytic activity of spinels for oxygen reduction by structure reversal, Angew. Chem., Int. Ed. 55 (2016) 1340–1344.

[12] S.S.A. Shah, T. Najam, C. Cheng, L. Peng, R. Xiang, L. Zhang, J. Deng, W. Ding, Z. Wei, Exploring Fe-Nx for peroxide reduction: template-free synthesis of Fe-Nx traumatized mesoporous carbon nanotubes as an ORR catalyst in acidic and alkaline solutions, Chem. Eur. J. 24 (2018) 10630–10635.

[13] W. Niu, L. Li, X. Liu, N. Wang, J. Liu, W. Zhou, Z. Tang, S. Chen, Mesoporous N-doped carbons prepared with thermally removable nanoparticle templates: an efficient electrocatalyst for oxygen reduction reaction, J. Am. Chem. Soc. 137 (2015) 5555–5562.

[14] L. Bu, C. Tang, Q. Shao, X. Zhu, X. Huang, Three-dimensional Pd3Pb nanosheet assemblies: high-performance non-Pt electrocatalysts for bifunctional fuel cell reactions, ACS Catal. 8 (2018) 4569–4575.

[15] C. Lei, H. Chen, J. Cao, J. Yang, M. Qiu, Y. Xia, C. Yuan, B. Yang, Z. Li, X. Zhang, L. Lei, J. Abbott, Y. Zhong, X. Xia, G. Wu, Q. He, Y. Hou, Fe-N4 sites embedded into carbon nanofiber integrated with electrochemically exfoliated graphene for oxygen evolution in acidic medium, Adv. Energy Mater. 8 (2018) 1801912.

[16] D. Yan, Y. Li, J. Huo, R. Chen, L. Dai, S. Wang, Defect chemistry of nonprecious-metal electrocatalysts for oxygen reactions, Adv. Mater. 29 (2017) 1606459.

[17] K.D. Gilroy, A. Ruditskiy, H.-C. Peng, D. Qin, Y. Xia, Bimetallic nanocrystals: syntheses, properties, and applications, Chem. Rev. 116 (2016) 10414–10472.

[18] Y. Luo, L.A. Estudillo-Wong, G. Cavillo, G. Granozzi, N. Alonso-Vante, An easy and cheap chemical route using a MOF precursor to prepare Pd–Cu electrocatalyst for efficient energy conversion cathodes, J. Catal. 338 (2016) 135–142.

[19] J. Wu, S. Shan, J. Luo, P. Joseph, V. Petkov, C.-J. Zhong, PdCu nanoalloy electrocatalysts in oxygen reduction reaction: role of composition and phase state in catalytic synergy, ACS Appl. Mater. Interfaces 7 (2015) 25906–25913.

[20] Y. Zheng, S. Zhao, S. Liu, H. Yin, Y.-Y. Chen, J. Bao, M. Han, Z. Dai, Component-controlled synthesis and assembly of Cu–Pd nanocrystals on graphene for oxygen reduction reaction, ACS Appl. Mater. Interfaces 7 (2015) 5347–5357.

[21] G. Bampos, S. Bebelis, D.I. Kondarides, X. Verykios, Comparison of the activity of Pd–M (M: Ag Co, Cu, Fe, Ni, Zn) bimetallic electrocatalysts for oxygen reduction reaction, Top. Catal. 60 (2017) 1260–1273.

[22] Y. Xiong, Y. Yang, F.J. DiSalvo, H.D. Abruña, Pt-decorated composition-tunable Pd–Fe@Pd/C core-shell nanoparticles with enhanced electrocatalytic activity toward the oxygen reduction reaction, J. Am. Chem. Soc. 140 (2018) 7248–7255.

[23] Z. Liu, X. Yang, L. Cui, Z. Shi, B. Lu, X. Guo, J. Zhang, L. Xu, Y. Tang, Y. Xiang, High-performance oxygen reduction electrocatalysis enabled by 3D PdNi nanocorals with hierarchical porosity, Part. Part. Syst. Charact. 35 (2017) 1700366.

[24] S. Liu, Q. Zhang, Y. Li, M. Han, L. Gu, C. Nan, J. Bao, Z. Dai, Five-fold twinned Pd2NiAg nanocrystals with increased surface Ni site availability to improve oxygen reduction activity, J. Am. Chem. Soc. 137 (2015) 2820–2823.

[25] H. Xue, J. Tang, H. Gong, H. Guo, X. Fan, T. Wang, J. He, Y. Yamauchi, Fabrication of PdCo bimetallic nanoparticles anchored on three-dimensional ordered N-doped porous carbon as an efficient catalyst for oxygen reduction reaction, ACS Appl. Mater. Interfaces 8 (2016) 20766–20771.

[26] C. Zhao, X. Yan, G. Wang, Y. Jin, X. Du, W. Du, L. Sun, C. Ji, PdCo bimetallic nano-electrocatalyst as effective air-cathode for aqueous metal-air batteries, Int. J. Hydrogen Energy 43 (2018) 5001–5011.

[27] H. Yin, S. Liu, C. Zhang, J. Bao, Y. Zheng, M. Han, Z. Dai, Well-coupled graphene and Pd-based bimetallic nanocrystals nanocomposites for electrocatalytic oxygen reduction reaction, ACS Appl. Mater. Interfaces 6 (2014) 2086–2094.

[28] Y. Zuo, D. Rao, S. Li, T. Li, G. Zhu, S. Chen, L. Song, Y. Chai, H. Han, Atomic vacancies control of Pd-based catalysts for enhanced electrochemical performance, Adv. Mater. 30 (2018).

[29] J. Wu, S. Shan, V. Petkov, B. Prasai, H. Cronk, P. Joseph, J. Luo, C.-J. Zhong, Composition–structure–activity relationships for palladium-alloyed nanocatalysts in oxygen reduction reaction: an ex-situ/in-situ high energy x-ray diffraction study, ACS Catal. 5 (2015) 5317–5327.

[30] L. Xiao, L. Zhuang, Y. Liu, J. Lu, H.D. Abruña, Activating Pd by morphology tailoring for oxygen reduction, J. Am. Chem. Soc. 131 (2009) 602–608.

[31] H. Zhang, M. Jin, Y. Xiong, B. Lim, Y. Xia, Shape-controlled synthesis of Pd nanocrystals and their catalytic applications, Acc. Chem. Res. 46 (2013) 1783–1794.

[32] M. Shao, J. Odell, M. Humbert, T. Yu, Y. Xia, Electrocatalysis on shape-controlled palladium nanocrystals: oxygen reduction reaction and formic acid oxidation, J. Phys. Chem. C 117 (2013) 4172–4180.

[33] M. Shao, T. Yu, J.H. Odell, M. Jin, Y. Xia, Structural dependence of oxygen reduction reaction on palladium nanocrystals, Chem. Commun. 47 (2011) 6566–6568.

[34] M. Shao, Q. Chang, J.-P. Dodelet, R. Chenitz, Recent advances in electrocatalysts for oxygen reduction reaction, Chem. Rev. 116 (2016) 3594–3657.

[35] Q. Xue, J. Bai, C. Han, P. Chen, J.-X. Jiang, Y. Chen, Au nanowires@Pd-polyethylenimine nanohybrids as highly active and methanol-tolerant

[36] Z. Liu, X. Yang, L. Cui, Z. Shi, B. Lu, X. Guo, J. Zhang, L. Xu, Y. Tang, Y. Xiang, High-performance oxygen reduction electrocatalysis enabled by 3D PdNi nanocorals with hierarchical porosity, Part. Part. Syst. Charact. 35 (2018) 1700366.

[37] D.J. You, D.H. Kim, J.R. De Lile, C. Li, S.G. Lee, J.M. Kim, C. Pak, Pd core-shell alloy catalysts for high-temperature polymer electrolyte membrane fuel cells: Effect of the core composition on the activity towards oxygen reduction reactions, Appl. Catal. A: Gen. 562 (2018) 250–257.

[38] S. Ma, M. Sadakiyo, M. Heima, R. Luo, R.T. Haasch, J.I. Gold, M. Yamauchi, P.J.A. Kenis, Electroreduction of carbon dioxide to hydrocarbons using bimetallic Cu–Pd catalysts with different mixing patterns, J. Am. Chem. Soc. 139 (2017) 47–50.

[39] H. Yang, Z. Tang, K. Wang, W. Wu, Y. Chen, Z. Ding, Z. Liu, S. Chen, Co@Pd core-shell nanoparticles embedded in nitrogen-doped porous carbon as dual functional electrocatalysts for both oxygen reduction and hydrogen evolution reactions, J. Colloid Interf. Sci. 528 (2018) 18–26.

[40] Q. Wang, L. Wang, Z. Tang, F. Wang, W. Yan, H. Yang, W. Zhou, L. Li, X. Kang, S. Chen, Oxygen reduction catalyzed by gold nanoclusters supported on carbon nanosheets, Nanoscale 8 (2016) 6629–6635.

[41] K.J.J. Mayrhofer, D. Strmcnik, B.B. Blizanac, V. Stamenkovic, M. Arenz, N.M. Markovic, Measurement of oxygen reduction activities via the rotating disc electrode method: From Pt model surfaces to carbon-supported high surface area catalysts, Electrochim. Acta 53 (2008) 3181–3188.

[42] W. He, H. Jiang, Y. Zhou, S. Yang, X. Xue, Z. Zou, X. Zhang, D.L. Akins, H. Yang, An efficient reduction route for the production of Pd–Pt nanoparticles anchored on graphene nanosheets for use as durable oxygen reduction electrocatalysts, Carbon 50 (2012) 265–274.

[43] D. Sebastián, A.G. Ruíz, I. Suelves, R. Moliner, M.J. Lázaro, V. Baglio, A. Stassi, A. S. Aricò, Enhanced oxygen reduction activity and durability of Pt catalysts supported on carbon nanofibers, Appl. Catal. B: Environ. 115–116 (2012) 269–275.

[44] H. Huang, K. Li, Z. Chen, L. Luo, Y. Gu, D. Zhang, C. Ma, R. Si, J. Yang, Z. Peng, J. Zeng, Achieving remarkable activity and durability toward oxygen reduction reaction based on ultrathin Rh-doped Pt nanowires, J. Am. Chem. Soc. 139 (2017) 8152–8159.

[45] Y. Cong, I.T. McCrum, X. Gao, Y. Lv, S. Miao, Z. Shao, B. Yi, H. Yu, M.J. Janik, Y. Song, Uniform Pd0.33Ir0.67 nanoparticles supported on nitrogen-doped carbon with remarkable activity toward the alkaline hydrogen oxidation reaction, J. Mater. Chem. A 7 (2019) 3161–3169.

[46] W. Wu, Y. Wu, D. Zheng, K. Wang, Z. Tang, Ni@Ru core-shell nanoparticles on flower-like carbon nanosheets for hydrogen evolution reaction at All-pH values, oxygen evolution reaction and overall water splitting in alkaline solution, Electrochim. Acta 320 (2019), 134568.

[47] J. Gardy, E. Nourafkan, A. Osatiashtiani, A.F. Lee, K. Wilson, A. Hassanpour, X. Lai, A core-shell SO4/Mg-Al-Fe3O4 catalyst for biodiesel production, Appl. Catal. B: Environ. 259 (2019), 118093.

[48] D. Cheng, Q. Zhong, J. Wang, Y. Bu, Amorphous core-shell nanoparticles as a highly effective and stable battery-type electrode for hybrid supercapacitors, Adv. Mater. Interfaces 6 (2019) 1900858.

[49] A.S. Malik, S.F. Zaman, A.A. Al-Zahrani, M.A. Daous, H. Driss, L.A. Petrov, Development of highly selective PdZn/CeO2 and Ca-doped PdZn/CeO2 catalysts for methanol synthesis from CO2 hydrogenation, Appl. Catal. A: Gen. 560 (2018) 42–53.

[50] Y. Lu, Y. Jiang, X. Gao, X. Wang, W. Chen, Strongly coupled Pd nanotetrahedron/tungsten oxide nanosheet hybrids with enhanced catalytic activity and stability as oxygen reduction electrocatalysts, J. Am. Chem. Soc. 136 (2014) 11687–11697.

[51] J.-N. Zheng, S.-S. Li, X. Ma, F.-Y. Chen, A.-J. Wang, J.-R. Chen, J.-J. Feng, Green synthesis of core–shell gold–palladium@palladium nanocrystals dispersed on graphene with enhanced catalytic activity toward oxygen reduction and methanol oxidation in alkaline media, J. Power Sources 262 (2014) 270–278.

[52] K. Gong, F. Du, Z. Xia, M. Durstock, L. Dai, Nitrogen-doped carbon nanotube arrays with high electrocatalytic activity for oxygen reduction, Science 323 (2009) 760–764.

[53] M. Friedrich, D. Teschner, A. Knop-Gericke, M. Armbrüster, Influence of bulk composition of the intermetallic compound ZnPd on surface composition and methanol steam reforming properties, J. Catal. 285 (2012) 41–47.

[54] M. Hu, S. Zhao, S. Liu, C. Chen, W. Chen, W. Zhu, C. Liang, W.-C. Cheong, Y. Wang, Y. Yu, Q. Peng, K. Zhou, J. Li, Y. Li, MOF-confined sub-2 nm atomically ordered intermetallic PdZn nanoparticles as high-performance catalysts for selective hydrogenation of acetylene, Adv. Mater. 30 (2018) 1801878.

[55] Y. Luo, Y. Sun, U. Schwarz, M. Armbrüster, Systematic exploration of synthesis pathways to nanoparticulate ZnPd, Chem. Mater. 24 (2012) 3094–3100.

[56] W. Xiao, M.A.L. Cordeiro, G. Gao, A. Zheng, J. Wang, W. Lei, M. Gong, R. Lin, E. Stavitski, H.L. Xin, D. Wang, Atomic rearrangement from disordered to ordered Pd-Fe nanocatalysts with trace amount of Pt decoration for efficient electrocatalysis, Nano Energy 50 (2018) 70–78.

[57] C.P. Deming, R. Mercado, V. Gadiraju, S.W. Sweeney, M. Khan, S. Chen, Graphene quantum dots-supported palladium nanoparticles for efficient electrocatalytic reduction of oxygen in alkaline media, ACS Sustainable Chem. Eng. 3 (2015) 3315–3323.

[58] C.P. Deming, R. Mercado, J.E. Lu, V. Gadiraju, M. Khan, S. Chen, Oxygen electroreduction catalyzed by palladium nanoparticles supported on nitrogen-

doped graphene quantum dots: impacts of nitrogen dopants, ACS Sustainable Chem. Eng. 4 (2016) 6580–6589.

[59] W. Yan, Z. Tang, L. Wang, Q. Wang, H. Yang, S. Chen, PdAu alloyed clusters supported by carbon nanosheets as efficient electrocatalysts for oxygen reduction, Int. J. Hydrogen Energy 42 (2017) 218–227.

[60] Z. Zong, K. Xu, D. Li, Z. Tang, W. He, Z. Liu, X. Wang, Y. Tian, Peptide templated Au@Pd core-shell structures as efficient bi-functional electrocatalysts for both oxygen reduction and hydrogen evolution reactions, J. Catal. 361 (2018) 168–176.

[61] Y. Feng, C. Yang, W. Fang, B. Huang, Q. Shao, X. Huang, Anti-poisoned oxygen reduction by the interface modulated Pd@NiO core@shell, Nano Energy 58 (2019) 234–243.

[62] Y. Cheng, S. Lu, W. Xu, H. Wen, J. Wang, Fabrication of superhydrophobic Au–Zn alloy surface on a zinc substrate for roll-down, self-cleaning and anti-corrosion properties, J. Mater. Chem. A 3 (2015) 16774–16784.

[63] L. Hu, B. Qu, C. Li, Y. Chen, L. Mei, D. Lei, L. Chen, Q. Li, T. Wang, Facile synthesis of uniform mesoporous ZnCo2O4 microspheres as a high-performance anode material for Li-ion batteries, J. Mater. Chem. A 1 (2013) 5596–5602.

[64] T.T. Vo Doan, J. Wang, K.C. Poon, D.C.L. Tan, B. Khezri, R.D. Webster, H. Su, H. Sato, Theoretical modelling and facile synthesis of a highly active boron-doped palladium catalyst for the oxygen reduction reaction, Angew. Chem., Int. Ed. 55 (2016) 6842–6847.

[65] L. Sun, B. Liao, X. Ren, Y. Li, P. Zhang, L. Deng, Y. Gao, Ternary PdNi-based nanocrystals supported on nitrogen-doped reduced graphene oxide as highly active electrocatalysts for the oxygen reduction reaction, Electrochim. Acta 235 (2017) 543–552.

[66] G. Wang, J. Guan, L. Xiao, B. Huang, N. Wu, J. Lu, L. Zhuang, Pd skin on AuCu intermetallic nanoparticles: A highly active electrocatalyst for oxygen reduction reaction in alkaline media, Nano Energy 29 (2016) 268–274.

[67] W. Yan, Z. Tang, Z. Li, L. Wang, H. Yang, Q. Wang, W. Wu, S. Chen, Ultrasmall palladium nanoclusters encapsulated in porous carbon nanosheets for oxygen electroreduction in alkaline media, ChemElectroChem 4 (2017) 1349–1355.

[68] T. Li, Z. Tang, K. Wang, W. Wu, S. Chen, C. Wang, Palladium nanoparticles grown on β-Mo2C nanotubes as dual functional electrocatalysts for both oxygen reduction reaction and hydrogen evolution reaction, Int. J. Hydrogen Energy 43 (2018) 4932–4941.

[69] T. Kar, R. Devivaraprasad, B. Bera, R. Ramesh, M. Neergat, Investigation on the reduction of the oxides of Pd and graphite in alkaline medium and the simultaneous evolution of oxygen reduction reaction and peroxide generation features, Electrochim. Acta 191 (2016) 81–89.

[70] Z. Yang, M. Chen, M. Xia, M. Wang, X. Wang, An effective and durable interface structure design for oxygen reduction and methanol oxidation electrocatalyst, Appl. Surf. Sci. 487 (2019) 655–663.

[71] S.M. Senthil Kumar, K. Selvakumar, R. Thangamuthu, One-pot hydrothermal synthesis of supported CoS electrocatalysts: The effect of support nature on oxygen reduction reaction activity in alkaline medium, Int. J. Hydrogen Energy 43 (2018) 4773–4783.

[72] C.P. Deming, A. Zhao, Y. Song, K. Liu, M.M. Khan, V.M. Yates, S. Chen, Alkyne-protected AuPd alloy nanoparticles for electrocatalytic reduction of oxygen, ChemElectroChem 2 (2015) 1719–1727.

[73] S. Hussain, N. Kongi, H. Erikson, M. Rähn, M. Merisalu, L. Matisen, P. Paiste, J. Aruväli, V. Sammelselg, L.A. Estudillo-Wong, K. Tammeveski, N. Alonso-Vante, Platinum nanoparticles photo-deposited on SnO2-C composites: An active and durable electrocatalyst for the oxygen reduction reaction, Electrochim. Acta 316 (2019) 162–172.

[74] C. Song, J. Zhang, PEM Fuel Cell Electrocatalysis and Catalyst Layers: Fundamentals and Applications, 2008th Edition, Springer, 2008, pp. 89–134.

[75] W. Xie, Z. Li, S. Jiang, J. Li, M. Shao, M. Wei, Mass-loading independent electrocatalyst with high performance for oxygen reduction reaction and Zn-air battery based on Co-N-codoped carbon nanotube assembled microspheres, Chem. Eng. J. 373 (2019) 734–743.

[76] M. Lüsi, H. Erikson, M. Merisalu, A. Kasikov, L. Matisen, V. Sammelselg, K. Tammeveski, Oxygen electroreduction in alkaline solution on Pd coatings prepared by galvanic exchange of copper, Electrocatal. 9 (2018) 400–408.

[77] Y. Li, S. Lin, X. Ren, H. Mi, P. Zhang, L. Sun, L. Deng, Y. Gao, One-step rapid in-situ synthesis of nitrogen and sulfur co-doped three-dimensional honeycomb-ordered carbon supported PdNi nanoparticles as efficient electrocatalyst for oxygen reduction reaction in alkaline solution, Electrochim. Acta 253 (2017) 445–454.

[78] J. Jiang, H. Gao, S. Lu, X. Zhang, C.-Y. Wang, W.-K. Wang, H.-Q. Yu, Ni–Pd core–shell nanoparticles with Pt-like oxygen reduction electrocatalytic performance in both acidic and alkaline electrolytes, J. Mater. Chem. A 5 (2017) 9233–9240.

[79] Y. Holade, R.G. da Silva, K. Servat, T.W. Napporn, C. Canaff, A.R. de Andrade, K.B. Kokoh, Facile synthesis of highly active and durable PdM/C (M = Fe, Mn) nanocatalysts for the oxygen reduction reaction in an alkaline medium, J. Mater. Chem. A 4 (2016) 8337–8349.

[80] K. Jiang, P. Wang, S. Guo, X. Zhang, X. Shen, G. Lu, D. Su, X. Huang, Ordered PdCu-based nanoparticles as bifunctional oxygen-reduction and ethanol-oxidation electrocatalysts, Angew. Chem., Int. Ed. 55 (2016) 9030–9035.

[81] D. Wang, H.L. Xin, R. Hovden, H. Wang, Y. Yu, D.A. Muller, F.J. DiSalvo, H.D. Abruña, Structurally ordered intermetallic platinum–cobalt core–shell nanoparticles with enhanced activity and stability as oxygen reduction electrocatalysts, Nat. Mater. 12 (2013) 81–87.

[82] W. Yan, W. Wu, K. Wang, Z. Tang, S. Chen, Oxygen reduction reaction and hydrogen evolution reaction catalyzed by carbon-supported molybdenum-coated palladium nanocubes, Int. J. Hydrogen Energy 43 (2018) 17132–17141.

[83] Yonggang Feng, Qi Shao, Yujin Ji, Xiaoneng Cui, Youyong Li, Xing Zhu, Xiaoqing Huang, Surface-modulated palladium-nickel icosahedra as high-performance non-platinum oxygen reduction electrocatalysts, Sci. Adv. 4 (7) (2018) eaap8817, https://doi.org/10.1126/sciadv.aap8817.

[84] J. Lu, W. Zhou, L. Wang, J. Jia, Y. Ke, L. Yang, K. Zhou, X. Liu, Z. Tang, L. Li, S. Chen, Core-shell nanocomposites based on gold nanoparticle@zinc–iron-embedded porous carbons derived from metal-organic frameworks as efficient dual catalysts for oxygen reduction and hydrogen evolution reactions, ACS Catal. 6 (2016) 1045–1053.